A&A 549, A16 (2013)
DOI: 10.1051/0004-6361/201220163
© ESO 2012

Astronomy & Astrophysics

Mapping water in protostellar outflows with *Herschel*⋆

PACS and HIFI observations of L1448-C⋆⋆

B. Nisini[1], G. Santangelo[1], S. Antoniucci[1], M. Benedettini[2], C. Codella[3], T. Giannini[1], A. Lorenzani[3], R. Liseau[4], M. Tafalla[5], P. Bjerkeli[4], S. Cabrit[6], P. Caselli[7,3], L. Kristensen[8], D. Neufeld[9], G. Melnick[10], and E. F. van Dishoeck[8,11]

[1] INAF – Osservatorio Astronomico di Roma, via di Frascati 33, 00040 Monte Porzio Catone, Italy
e-mail: nisini@oa-roma.inaf.it
[2] INAF – Istituto di Astrofisica e Planetologia Spaziali, via Fosso del Cavaliere 100, 00133 Roma, Italy
[3] INAF Osservatorio Astrofisico di Arcetri, Largo E. Fermi 5, 50125 Firenze, Italy
[4] Department of Earth and Space Sciences, Chalmers University of Technology, Onsala Space Observatory, 439 92 Onsala, Sweden
[5] Observatorio Astronómico Nacional (IGN), Alfonso XII 3, 28014 Madrid, Spain
[6] LERMA, Observatoire de Paris, UMR 8112 CNRS, 61 Av. de l'Observatoire, 75014 Paris, France
[7] School of Physics and Astronomy, University of Leeds, Leeds LS2 9JT, UK
[8] Leiden Observatory, Leiden University, PO Box 9513, 2300 RA Leiden, The Netherlands
[9] Department of Physics and Astronomy, Johns Hopkins University, 3400 North Charles Street, Baltimore, MD 21218, USA
[10] Harvard-Smithsonian Center for Astrophysics, 60 Garden Street, MS 42, Cambridge, MA 02138, USA
[11] Max Planck Institut fur Extraterrestrische Physik, Giessenbachstrasse 1, 85748 Garching, Germany

Received 3 August 2012 / Accepted 26 October 2012

ABSTRACT

Context. Water is a key probe of shocks and outflows from young stars because it is extremely sensitive to both the physical conditions associated with the interaction of supersonic outflows with the ambient medium and the chemical processes at play.
Aims. Our goal is to investigate the spatial and velocity distribution of H_2O along outflows, its relationship with other tracers, and its abundance variations. In particular, this study focuses on the outflow driven by the low-mass protostar L1448-C, which previous observations have shown to be one of the brightest H_2O emitters among the class 0 outflows.
Methods. To this end, maps of the o-H_2O 1_{10}–1_{01} and 2_{12}–1_{01} transitions taken with the *Herschel*-HIFI and PACS instruments, respectively, are presented. For comparison, complementary maps of the CO(3–2) and SiO(8–7) transitions, obtained at the JCMT, and the H_2 S(0) and S(1) transitions, taken from the literature, were used as well. Physical conditions and H_2O column densities were inferred using large velocity gradient radiative transfer calculations.
Results. The water distribution appears to be clumpy, with individual peaks corresponding to shock spots along the outflow. The bulk of the 557 GHz line is confined to radial velocities in the range ±10–50 km s^{-1}, but extended emission at extreme velocities (up to $v_r \sim 80$ km s^{-1}) is detected and is associated with the L1448-C extreme high-velocity (EHV) jet. The H_2O 1_{10}–1_{01}/CO(3–2) ratio shows strong variations as a function of velocity that likely reflect different and changing physical conditions in the gas that is responsible for the emissions from the two species. In the EHV jet, a low H_2O/SiO abundance ratio is inferred, which could indicate molecular formation from dust-free gas directly ejected from the proto-stellar wind. The ratio between the two observed H_2O lines and the comparison with H_2 indicate *averaged* $T_{\rm kin}$ and $n(H_2)$ values of ~300–500 K and 5×10^6 cm^{-3}, respectively, while a water abundance with respect to H_2 of about $0.5–1 \times 10^{-6}$ along the outflow is estimated, in agreement with results found by previous studies. The fairly constant conditions found all along the outflow imply that evolutionary effects on the timescales of outflow propagation do not play a major role in the H_2O chemistry.
Conclusions. The results of our analysis show that the bulk of the observed H_2O lines comes from post-shocked regions where the gas, after being heated to high temperatures, has already been cooled down to a few hundred K. The relatively low derived abundances, however, call for some mechanism that diminishes the H_2O gas in the post-shock region. Among the possible scenarios, we favor H_2O photodissociation, which requires the superposition of a low-velocity nondissociative shock with a fast dissociative shock able to produce a far-ultraviolet field of sufficient strength.

Key words. stars: formation – stars: winds, outflows – ISM: abundances – ISM: molecules – ISM: jets and outflows – ISM: individual objects: L1448

1. Introduction

The earliest stages of star formation are characterized by strong mass loss, which is at the origin of observationally prominent phenomena, such as shocks and molecular outflows. The high velocity of the shocked gas and the elevated gas temperature strongly modify the chemical composition of the gas. Depending upon the initial conditions, processes that alter the gas composition include gas dissociation and ionization, high-temperature chemical reactions and dust grain reprocessing (e.g. Flower et al. 2010). These processes produce observable signatures in the form of emission from specific molecular and/or atomic lines, the study of which is crucial not only as a probe of the shock chemistry, but also for understanding the complex interaction between wind/jet-shocks and large-scale outflows.

⋆ *Herschel* is an ESA space observatory with science instruments provided by European-led Principal Investigator consortia and with important participation from NASA.
⋆⋆ Appendices are available in electronic form at http://www.aanda.org

Among the different tracers, lines of H_2 and CO are routinely used to infer the physical conditions and the dynamics of shocked gas, while less abundant molecules, such as SiO or CH_3OH are sensitive to the chemical processes triggered in the shocked gas. In this framework, water can be considered a key molecule: in fact, the H_2O relative line intensities and its column density are subject to strong variations that are highly dependent on the actual physical conditions of the gas but also on its thermal and chemical history. This is because the water abundance strongly depends on the mechanism of evaporation/freeze-out in grain mantles and the endothermic gas-phase chemical reactions that drive all free oxygen into water, as well as on the relative timescales of these processes (e.g. Bergin et al. 1998; Flower & Pineau des Forêts 2010).

Observations obtained with the Infrared Space Observatory (ISO) have been the first to detect H_2O emissions from states of relatively high excitation ($T_{\rm kin} \sim$ 500–1500 K, e.g. Liseau et al. 1996; Ceccarelli et al. 1998; Nisini et al. 2000). More recently, the SWAS and *Odin* satellites observed the fundamental o-H_2O transition at 557 GHz in a sample of outflows (Bjerkeli et al. 2009; Franklin et al. 2008). These observations probed cooler gas than had been observed with ISO, but were able to resolve the line profiles for the first time, demonstrating the association of water emission with the high-velocity gas. These studies provided the first determinations of the water abundance, yielding values in the range $\sim 10^{-7}$ to $\sim 10^{-4}$ and suggesting that the H_2O abundance depends on the gas temperature and speed (Franklin et al. 2008; Giannini et al. 2001). However, the strength of this conclusion was limited by the large beam sizes used in these previous observations, together with their limited spectral resolution and/or excitation coverage; these limitations made it difficult to associate enhanced abundances or broadened line profiles with specific regions along the outflows or to infer whether these globally averaged properties are really representative of the physical and chemical conditions in specific regions of shock activity.

Herschel (Pilbratt et al. 2010) represents the natural evolution for the study of H_2O in protostellar sources, thanks to the combination of much improved spectral/spatial resolution and sensitivity provided by the Photodetecting Array Camera and Spectrometer (PACS, Poglitsch et al. 2010) and Heterodyne Instrument for the Far Infrared (HIFI, de Graauw et al. 2010) instruments. In the framework of the "Water In Star-forming regions with *Herschel*" (WISH, van Dishoeck et al. 2011) key program, we have undertaken systematic PACS and HIFI observations of young outflows in nearby clouds. Within this program, studies of individual shocks have been published in Bjerkeli et al. (2011), Santangelo et al. (2012), Vasta et al. (2012), and Tafalla et al. (2012), while water maps of the L1157 and VLA1623 outflows have been presented in Nisini et al. (2010) and Bjerkeli et al. (2012). All these studies complement observations at the central source position, which probe outflowing gas shocked in the inner jet and envelope cavity walls (Kristensen et al. 2012; Herczeg et al. 2011; Kaska et al. 2012; Goicoechea et al. 2012).

This paper focuses on PACS and HIFI mapping observations of the outflow from the class 0 source L1448-C (also named L1448-mm). This is a low-luminosity ($L = 7.5\ L_\odot$; Tobin et al. 2007) protostellar source located in the Perseus Molecular Cloud ($D = 232$ pc; Hirota et al. 2011), which drives a powerful and highly collimated flow that has been detected through interferometric CO and SiO observations (Guilloteau et al. 1992; Bachiller et al. 1995; Hirano et al. 2010). To the north, the L1448-C outflow interacts with two more compact flows that originate from a small cluster of three young sources (L1448-NA, NB and NW, Looney et al. 2000).

Regions of shocked gas are seen along the entire outflow by means of near- and mid-IR molecular hydrogen emission (Davis & Smith 2006; Neufeld et al. 2009; Giannini et al. 2011), which indicate the presence of a gas in a wide range of temperatures, from ~300 to more than 2000 K. ISO detected a far-IR spectrum rich in H_2O and CO transitions toward the L1448-C outflow (Nisini et al. 1999, 2000). The analysis of these lines constrained their emission as coming from warm gas with an enhanced water abundance, as predicted by models for nondissociative shocks. SWAS and *Odin* detected the 557 GHz line but at a single-to-noise ratio that was too low to characterize its emission kinematically. These studies, however, suggest that this line might probe a colder water gas component whose abundance is less enhanced with respect to the warm gas (Benedettini et al. 2002). HDO emission at 80.6 GHz has also been detected toward L1448-C, and is associated with the protostar and the shocked walls of the outflow cavity (Codella et al. 2010b).

Within the WISH program, the L1448-C outflow has been the subject of a detailed study that includes a survey of several lines at specific positions in addition to the mapping observations presented here. In particular, *Herschel*-HIFI observations of the central L1448-C source have been reported by Kristensen et al. (2011), who detected prominent emission originating from a broad velocity component, probably associated with the interaction of the outflow with the protostellar envelope, and from the extreme high-velocity gas (EHV, the so-called "bullets") associated with the collimated molecular jet. Santangelo et al. (2012) discussed HIFI observations carried out toward two specific shock spots and showed that H_2O line profiles change significantly with excitation, indicating the presence of gas components having different physical conditions.

The main aims of this work will be to define the global morphological and kinematical properties of the H_2O emission in comparison with other standard outflow and shock tracers and to study abundance variations in the different shocked regions. To this end, complementary CO(3–2) and SiO(8–7) maps of the same region covered by the *Herschel* observations will be presented and discussed.

2. Observations

2.1. PACS observations

Observations with the PACS instrument were performed on 27 February 2010 (with observing identification number OBSID = 1342191349). The PACS integral field unit (IFU) in line spectroscopy mode was used in chopping/nodding mode to obtain a spectral map of the L1448 outflow centered on the H_2O 2_{12}–1_{01} line at 179.527 μm (i.e. 1669.905 GHz, hereafter referred to as the "179 μm line"). The IFU consists of a 5 × 5 pixel array providing a spatial sampling of 9.″4/pixel, for a total field of view of 47″ × 47″. The diffraction-limited full width at half maximum (FWHM) beam size at 179 μm is 12.″6. The L1448 outflow region (about 5′ × 2′ centered on the L1448-C(N) source, α(J2000) = $03^{\rm h}25^{\rm m}38.4^{\rm s}$, δ(J2000) = +30°44′06″) was covered through a single Nyquist-sampled raster map, arranged along the outflow axis. The *Herschel* pointing accuracy is ~2″.

The spectral resolution at 179 μm is $R \sim 1500$ (i.e. ~210 km s^{-1}). The observation was performed with a single scan cycle, providing an integration time per spectral resolution element of 30 s. The total on-source time for the entire map was 5670 s.

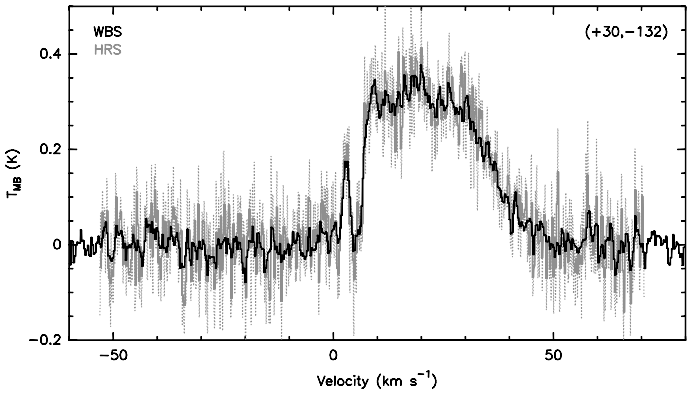

Fig. 1. Comparison between a WBS and HRS spectrum at a representative position in the outflow (offsets in arcsec with respect to L1448-C are indicated). Full black lines show the WBS data, while the gray dotted and full lines show the HRS data before and after smoothing to the WBS resolution, respectively.

The data were reduced with HIPE[1] v6.0, where they were flat-fielded and flux-calibrated by comparison with observations of Neptune. The calibration uncertainty amounts to around 20–30%, based on cross-calibrations with HIFI and PACS continuum photometry (internal WISH report). Finally, in-house IDL routines were used to locally fit and remove the continuum emission and to construct an integrated line map.

2.2. HIFI observations

A region of 5′ × 2′ oriented along the direction of the L1448 outflow (PA 164°) was mapped in the H_2O 1_{10}–1_{01} line at 556.936 GHz (i.e. 538.29 μm, hereafter "the 557 GHz line") with the HIFI instrument on 19 August 2010 (OBSID: 1342203200). The on-the-fly (OTF) mode was adopted, with a distance between adjacent scans of 16″, slightly less than half the diffraction HPBW (which is 38″ at the observed line frequency). The observations were performed in band 1b with both the Wide Band (resolution 1.1 MHz) and High Resolution (resolution 0.25 MHz) Spectrograph backends (WBS and HRS, respectively), for a total on-source integration time of 3981 s. An inspection of the two sets of data showed that the HRS spectra fail to provide additional information on the line velocity structure, and, furthermore, result in a higher rms noise when smoothed to the resolution of the WBS data (see an example in Fig. 1). Hence we only used the WBS data here. The data were reduced using HIPE v7, while the analysis was performed using the GILDAS[2] package. Calibration of the raw data onto the T_A scale was performed by the in-orbit system, while the spectra were converted to a T_{mb} scale adopting a main beam efficiency η_{mb} = 0.75 (Roelfsema et al. 2012).

Additional analysis consisted of baseline removal in each individual spectrum, averaging of spectra taken during different cycles, and construction of a final data-cube sampled at a regular grid with a half-beam spacing. Observations from the H and V polarizations were separately reduced: spectra from the two polarizations were acquired at slightly different coordinates (offset of ∼7″) that were taken into account in constructing the final regridded map. The rms noise achieved in the final data-cube is typically about T_{mb} ∼ 0.02 K in a 1 km s^{-1} bin.

2.3. JCMT-HARP observations

Complementary CO(3–2) and SiO(8–7) OTF maps were obtained in January 2009 with the HARP-B heterodyne array (Smith et al. 2008) and ACSIS correlator (Dent et al. 2000) on the James Clerk Maxwell Telescope (JCMT). The rest frequencies are 345 796.0 and 347 330.6 GHz for CO(3–2) and SiO(8–7), respectively (Pickett et al. 1998). The mapped area was covered by consecutive scans in basket-weave mode at a position angle of 160°. Each scan was offset by 29.″1 in the orthogonal direction, and the signal was integrated every 7.″3 (half HPBW, about 14″) along the scan direction. We observed in standard position-switched observing mode, with an off-source position at (+140″, 0″), chosen to be devoid of sources and the presence of high-velocity gas. Single maps were co-added and initial data cubes converted into GILDAS format for baseline subtraction and subsequent data analysis. The resulting map is centered on α_{J2000} = 03^{h}25^{m}38.^{s}9 δ_{J2000} = +30°44′05.″0, and it has dimensions of 300″ × 116″.

The observed bandwidth, 1 GHz, was sampled with 2048 channels for a spectral resolution of 488 kHz, which corresponds to 0.42 km s^{-1} at the observed frequencies. The spectra were smoothed to 1 km s^{-1} resolution to increase the sensitivity and converted to the main-beam brightness temperature (T_{mb}) scale adopting a main-beam efficiency (η_{mb}) of 0.6. The mean rms noise in T_{mb} is around 100 mK and 80 mK for CO(3–2) and SiO(8–7), respectively.

3. Results

3.1. H_2O morphology

The PACS line map displayed in Fig. 2 shows that the 179 μm emission is confined along the L1448-C outflow, with emission peaks roughly located at the positions of shocked spots previously identified through CO and SiO observations; these are named, following the nomenclature of Bachiller et al. (1990), R1 to R4 and B1 to B3 for the redshifted and blueshifted lobes, respectively. The strongest peak is observed toward the central position, where two IR sources, L1448-C(S) and C(N), are located (Jørgensen et al. 2006). Another strong emission peak is also observed in the terminal part of the redshifted lobe (knot R4). To the north, three different protostellar sources are present, resolved by mm interferometric observations and called A, B, and W, following Looney et al. (2000) and Kwon et al. (2006). H_2O emission ends abruptly at the position of L1449 N(A) and N(B), while a lane of water in absorption is seen toward L1448 N(W). Noticeably, and in contrast to what is observed at the central position, no emission is associated with any of the three L1448 N sources. Given the low spectral resolution of the PACS observations, there could be a mixture of emission and absorption beyond the B2 knot that causes a near cancellation of the emission. Figure 3 shows the line brightness profile along the flow, obtained by integrating the intensity in a region with a width of about 30″ perpendicular to the outflow axis. This plot shows the relative intensities of the different emission peaks, indicating that the emission is extended but clumpy.

In the same figure, bottom panel, an enlargement around the L1448-C source is displayed, where the 179 μm line and continuum intensity profiles are compared. In the continuum, the two sources C(S) and C(N) are spatially unresolved: the FWHM of

[1] HIPE is a joint development by the *Herschel* Science Ground Segment Consortium, consisting of ESA, the NASA *Herschel* Science Center, and the HIFI, PACS and SPIRE consortia.

[2] http://www.iram.fr/IRAMFR/GILDAS/

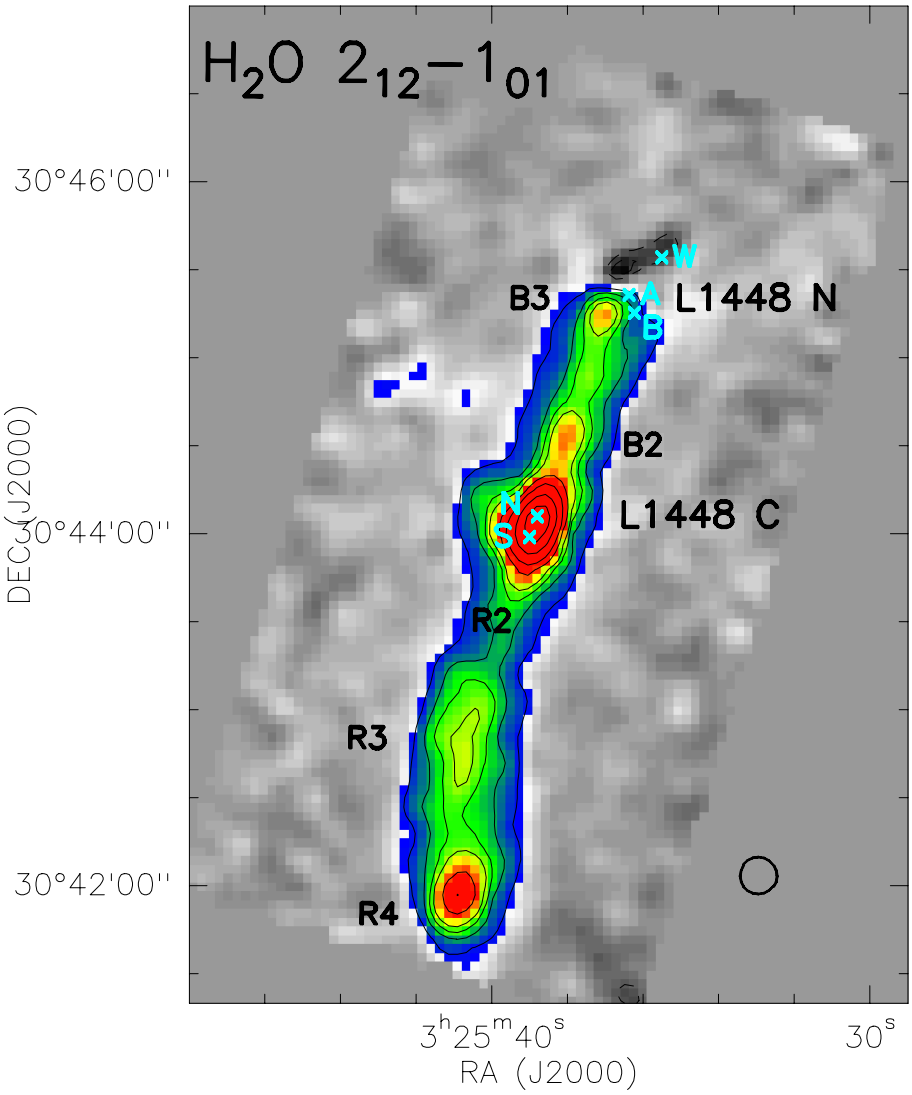

Fig. 2. Continuum-subtracted PACS map of the integrated H_2O 2_{12}–1_{01} emission along the L1448 outflow. Sources in the region are indicated with crosses: L1448-C(S) and C(N) in the central region, and L1448 NA, NB, and NW in the northern region. The diffraction-limited beam of *FWHM* 12.6″ is also indicated. The different emission peaks are labeled following the nomenclature adopted by Bachiller et al. (1990) for individual CO peaks. The average rms noise in the observed region is of about 2×10^{-6} erg s^{-1} cm^{-2} sr^{-1}. Contours are drawn at 3σ, 6σ, 9σ, 12σ, 16σ, 30σ, 50σ, and 75σ. Negative contours are indicated by dashed lines.

the spatial profile, when fitted with a Gaussian, is ∼18″, which means a deconvolved size of ∼13″, assuming both the beam and the emitting region to be Gaussian. For comparison, the two sources have a separation of about 8″. The line emission appears to be slightly extended with respect to the continuum, with a deconvolved FWHM of about 15″. This is roughly similar to the extension of the inner EHV SiO jet as observed, for example, by Guilloteau et al. (1992) and Hirano et al. (2010; their knots B1/R1). A more detailed description of the water morphology in comparison with other tracers in the regions around the C and N sources is given in Appendix A.

Figure 4, right panel, presents a comparison of the 179 μm emission, shown as a gray-scale image, with the integrated H_2O 557 GHz emission, displayed by separate contours for the blue- and redshifted emission. The two lines show a similar morphology compatible with the much lower spatial resolution of the HIFI spectra. Indeed, as in the PACS data, bright emission is observed toward the central L1448-C position and the southern redshifted outflow lobe, while no water emission is detected north of the L1448-N position. The complete set of HIFI data are presented in Fig. B.1, where all spectra are displayed in a regular grid. The comparison between the water and CO peaks can be directly visualized in Fig. 4, left panel, where the 179 μm line map is overlaid with contours of the CO(3–2) emission, separated into the blue- and redshifted gas. Along the southern outflow, the CO emission is systematically shifted with respect to H_2O. In the northern region, CO extends farthest to the north, where the outflow from the C(N) source is confused with a second outflow (at PA roughly 110°) emerging from the N(B) source (Bachiller et al. 1990, see next subsection). Therefore, although water roughly follows the direction of the CO outflow, there is no strict correlation between individual emission peaks.

3.2. H_2O kinematics

HIFI 557 GHz line profiles at selected positions along the outflows are shown in Fig. 5 and are compared with the CO(3–2) line. To make the comparison independent of beam filling effects, the CO(3–2) lines were extracted from a map convolved to the same spatial resolution as the H_2O 557 GHz observations. All lines show narrow absorption at the systemic velocity due to foreground gas. The 557 GHz line always traces the same range of velocity as CO. Maximum velocities up to 50 km s^{-1} are detected in all positions, while velocities reaching up to +80 km s^{-1} are observed at the position of the L1448-C source. Although they trace the same velocity range, the H_2O line profiles are different from those of CO, as already shown in other studies (Santangelo et al. 2012; Kristensen et al. 2011): most of the CO emission is localized at low velocity ($V_r - V_{LSR} \lesssim \pm 10$ km s^{-1}),

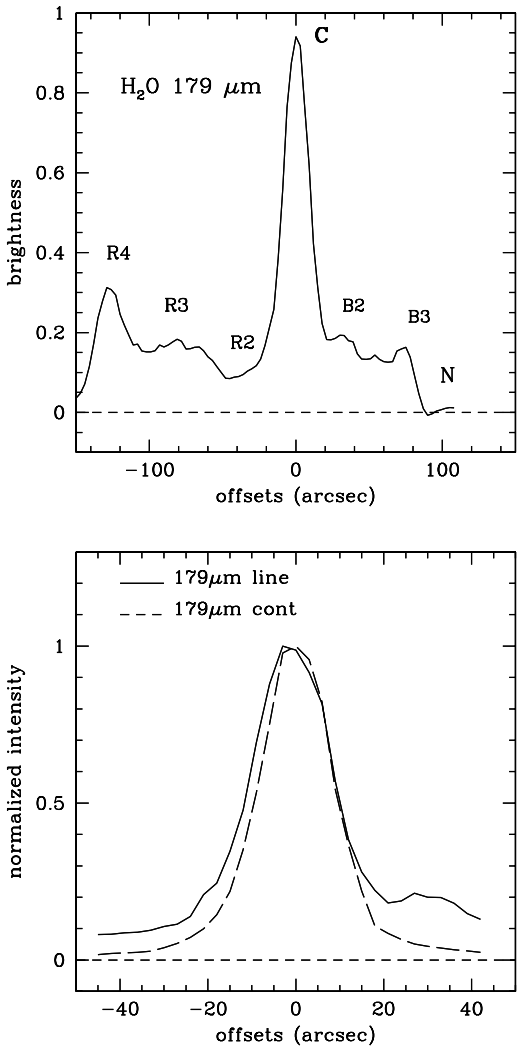

Fig. 3. *Upper panel*: H_2O 179 μm intensity cut along the L1448 flow, at PA 164°. The normalized intensity is integrated over a width of 30″ perpendicular to the cut. The location of the C(N) source is taken as the reference for the offsets. *Bottom panel*: normalized intensities of the 179 μm H_2O line and continuum around the L1448-C source, along the same cut direction as above.

while the bulk of the water emission occurs at intermediate velocities ($V_r - V_{LSR} \sim$ 5–30 km s^{-1}).

A detailed view of the H_2O and CO emission spatial distribution as a function of velocity can be visualized in the velocity channel maps presented in Fig. B.2. Figure 7 shows the maps of the two emissions integrated in three representative velocity intervals, corresponding to the low (±1–10 km s^{-1}), intermediate (±11–45 km s^{-1}), and high (±46–86 km s^{-1}) velocity gas. Emission at the low and intermediate velocities is detected all along the outflow, with the exception, as already noted from the PACS map, of the region northwest of the L1448-N sources, where water is absent while CO is detected. Figure 7 also shows that both H_2O and CO in the high-velocity range ($\gtrsim$50 km s^{-1}) are not confined at the central source position, but extend between −100 and +50 arcsec from L1448-C. If we look at the individual spectra shown in Fig. 5, we see that in the CO profiles this EHV gas always appears as a separate "bullet" emission superimposed on the line wing at lower velocity (e.g. Bachiller et al. 1990). These EHV bullets are physically associated with the highly collimated molecular jet displaced along the outflow axis (e.g. Hirano et al. 2010). Water emission kinematically associated with these bullets is clearly detected only toward the central L1448-C region (see Fig. 6) and has been discussed in Kristensen et al. (2011). Although EHV emission is also detected at greater distances from the source in CO, this emission does not appear as a separate bullet component in the individual H_2O spectra, but rather as an extension of the low-velocity component wing. Hence the contribution of the EHV gas to the total H_2O line emission is lower than in the case of CO. This will be discussed in more detail in the next section.

3.3. H_2-to-CO ratio vs. velocity

As seen in the previous section, the water and CO profiles look different, and thus their ratio varies significantly with velocity as illustrated in Fig. 5. At all selected outflow positions, the H_2O 1_{10}–1_{01}/CO(3–2) ratio increases with velocity up to $v \lesssim 20$ km s^{-1}: this is a trend that was identified previously in all sources observed in the 557 GHz line by SWAS and *Herschel* (Franklin et al. 2008; Kristensen et al. 2012). Given the high signal-to-noise ratio reached in our observations at high velocity, we can now see that beyond 20 km s^{-1} the ratio reaches a plateau and then decreases again at the highest velocities. Variations of the H_2O/CO line ratio could be caused by variations in the physical conditions with velocity and/or abundance variations. In addition, at velocities close to the ambient velocity, a different degree of absorption of the two lines by the cold gas may influence this ratio. The increase in the H_2O/CO ratio as a function of velocity has so far been interpreted as an increase of the H_2O abundance at high speeds; assuming the same temperature and density conditions for the two lines, Franklin et al. (2008) derived an H_2O abundance in the gas with $V_{max} \sim 20$ km s^{-1} an order of magnitude higher than that in the low-velocity gas. This conclusion, however, was based on an erroneous assumption, since different physical conditions pertain to CO and H_2O; moreover, the physical conditions change with velocity, as shown in, e.g., Santangelo et al. (2012); Vasta et al. (2012); Lefloch et al. (2010).

Furthermore, the decrease of the H_2O/CO line ratio at velocities higher than ~30–40 km s^{-1} contradicts the conclusion that a higher water abundance is always associated with the gas at the highest velocity. The drop in the H_2O/CO line ratio roughly coincides with the velocity range of the EHV bullet emission, indicating that a critical change in the physical and/or chemical conditions occurs in the bullets with respect to the "standard" wing emission. Tafalla et al. (2010) studied the chemical composition of the EHV gas in L1448, comparing it with the gas responsible for the wing emission, and found significant differences between these two components. They found, in particular, that the EHV gas is relatively rich in O-bearing species and poor in C-bearing molecules compared to the wing regime. Thus the observed drop in the H_2O 1_{10}–1_{01}/CO(3–2) ratio in the EHV regime is more easily understood if the water-emitting EHV gas has a lower temperature and/or density than the gas responsible for the wing emission. Kristensen et al. (2011) compared the excitation conditions for water in the EHV gas with those responsible for the wing emission toward the central position, but were unable to identify significant differences in the two regimes. Santangelo et al. (2012), on the other hand, found that at the L1448-R4 position the high-velocity H_2O emission is associated with gas at a density about an order of magnitude lower than that of the gas responsible for the low-velocity emission.

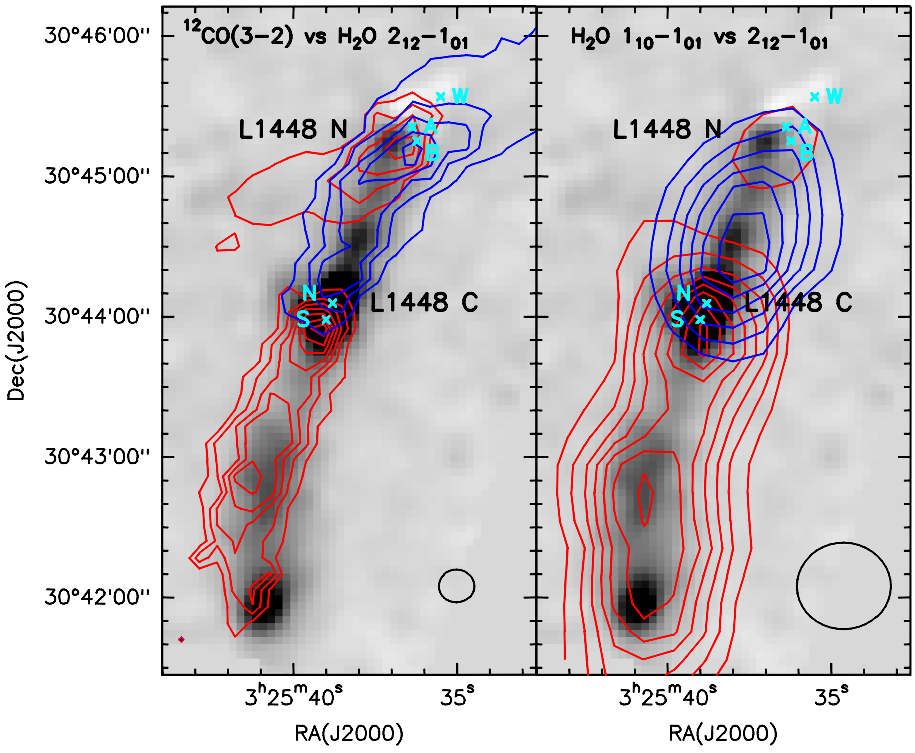

Fig. 4. Overlay of the JCMT ^{12}CO(3–2) (*left panel*) and HIFI H_2O 557 GHz (*right panel*) emission on the H_2O 179 μm map. The blue and red contours represent emission integrated in the velocity ranges (−100, +4) and (+6, +100) km s^{-1}, respectively. Contours are drawn from 25 to 200 K km s^{-1}, with steps of 20 K km s^{-1}, for the CO(3–2) map, and from 2 to 12 K km s^{-1}, with steps of 1.2 K km s^{-1}, for the H_2O 557 GHz map. The HPBW of 14″ (JCMT) and 38″ (HIFI) is indicated.

3.4. SiO and H_2O

The SiO(8–7) map, obtained together with the CO(3–2) observations, only shows emission close to the central position, where it can be associated with the L1448-C molecular jet (Hirano et al. 2010). In fact, while SiO emission from the (1–0) and (2–1) transitions is observed along the entire molecular outflow, peaking at the different clump positions (Bachiller et al. 1991; Dutrey et al. 1997), lines at higher excitation are observed only toward the highly collimated micro-jet (Bachiller et al. 1991; Nisini et al. 2007). The comparison of the SiO and H_2O emissions (see Fig. 6) shows that their profiles are strikingly different. The EHV bullets are more prominent in SiO than in H_2O: conversely, no SiO is associated with the strong intermediate velocity broad H_2O emission peaking around the ambient velocity. The association of SiO emission with the EHV collimated jet is a well-known feature characteristic of several class 0 sources (e.g. Hirano et al. 2006; Codella et al. 2007); it has been suggested that SiO in the jet is either directly synthesized in the dust-free jet acceleration region (Glassgold et al. 1991; Panoglou et al. 2011) or originates in shocked ambient material where silicon is released into the gas phase by the disruption of grain cores (e.g. Gusdorf et al. 2008).

An origin in the primary jet has recently been supported by both interferometric observations in the HH212 object (Cabrit et al. 2007) and by the molecular survey conducted on the L1448-R2 EHV bullet by Tafalla et al. (2010), who showed that the bullets possess a peculiar chemistry with respect to the standard outflow wing emission, suggesting an origin different from shocks. The fact that SiO(8–7) is more prominent than H_2O 557 GHz in the EHV bullets may either be an excitation effect or the result of an enhanced SiO/H_2O abundance ratio, or both. The excitation of SiO in the EHV bullets has been studied by Nisini et al. (2007), who found that the SiO-emitting gas has a density $\sim 10^6$ cm^{-3} and $T_{\rm kin} \gtrsim 300$ K. Kristensen et al. (2011) found that similar conditions may be consistent also with the water emission in the bullets, suggesting that SiO and H_2O are excited in the same gas. With this assumption, the observed H_2O 557 GHz/ SiO(8–7) intensity ratio in the bullets implies a H_2O/SiO abundance ratio of ∼10. Shock models that take the erosion of Si from grain cores and mantles into account predict this ratio to be about 10^3 or more, depending on the shock velocity (Gusdorf et al. 2008; Jiménez-Serra et al. 2008). On the other hand, a H_2O/SiO ratio of about 10 is predicted by the wind model of Glassgold et al. (1991) where H_2O and SiO are formed in dust-free gas directly ejected from the protostar, provided that the mass loss rate of the spherical wind is $>10^{-5}$ $M_\odot$ yr^{-1}. Only high mass loss rates like this yield a density at the wind base that is sufficiently high to permit efficient SiO synthesis through gas-phase reactions. Indeed, timescales for SiO production are rather low, i.e. they stay below 10^2 yr, for $T > 400$ K, only if the gas density is $\gtrsim 10^7$–10^8 cm^{-3}. Dionatos et al. (2009) measured a molecular mass flux rate of $\sim 10^{-7}$ $M_\odot$ yr^{-1} for the L1448 jet: for this low mass loss value, the model by Glassgold et al. (1991) predicts a negligible abundance of both SiO and H_2O. However, given the high collimation of the L1448 jet, the mass loss rate values are not directly comparable and it certainly cannot be ruled out that the two molecules trace the primary jet. In this respect, initial results presented in Panoglou et al. (2011) for the molecular survival in disk winds seem promising, predicting that a significant fraction of water is synthesized in jets from class 0 sources with a mass accretion rate of 5×10^{-6} $M_\odot$ yr^{-1}, implying a mass flux rate of about that measured in L1448. Finally, we note that the timescales to increase the water abundance to values $X(H_2O) > 10^{-5}$ in a gas with $T > 400$ K are about 100 yr (Bergin et al. 1998), which agrees well with the dynamical timescale for the L1448 jet propagation of about ∼150 yr (Hirano et al. 2010).

With regard to the broad H_2O emission at intermediate velocities, Kristensen et al. (2011) suggested an origin in shocks caused by the interaction between the outflow and the envelope. Such shocks would be expected to produce significant SiO emission, since the disruption of grain cores occurs at shock speeds $\gtrsim$25–30 km s^{-1} (Jiménez-Serra et al. 2008; Gusdorf et al. 2008). The efficiency of sputtering and grain-grain collisions, however,

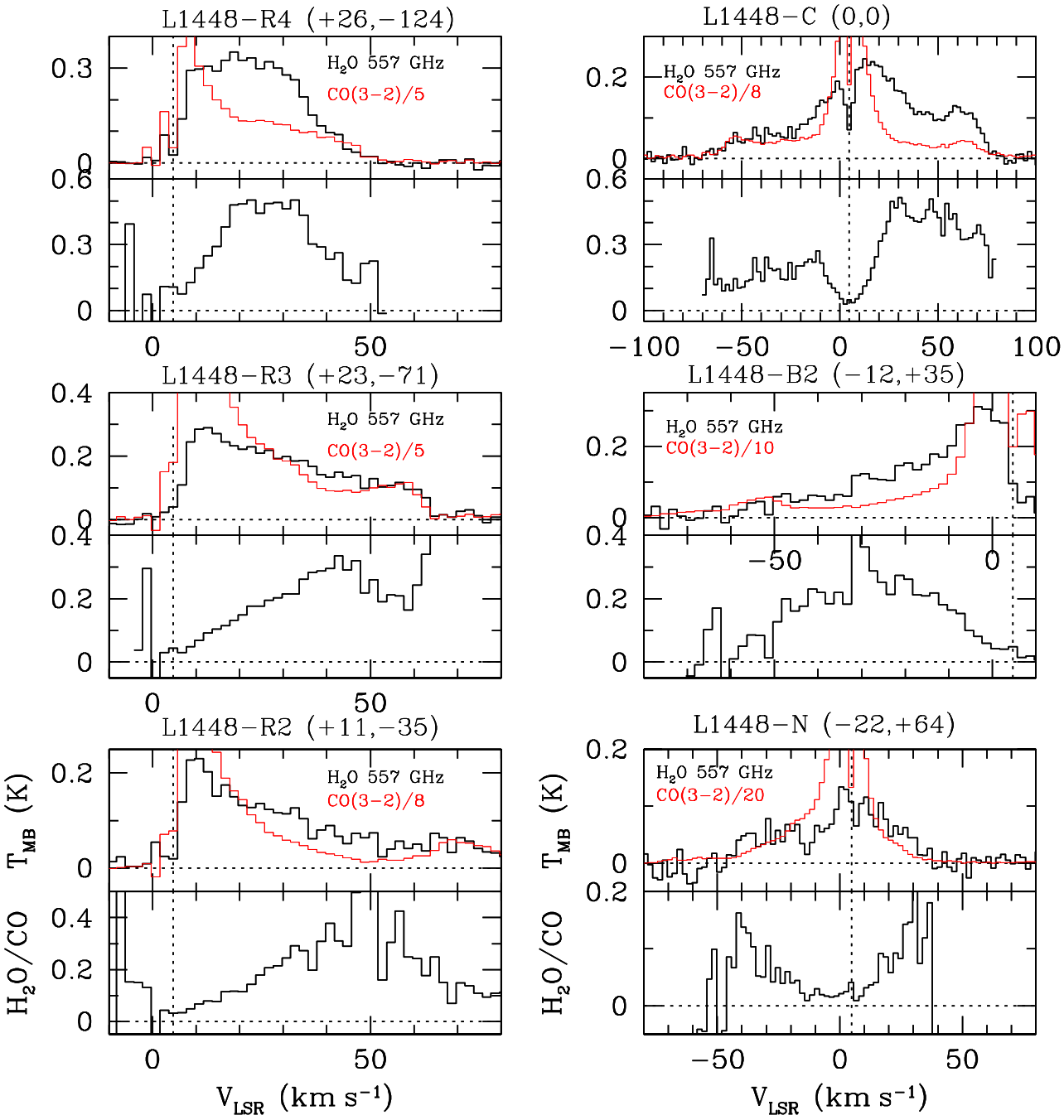

Fig. 5. H_2O 1_{10}–1_{01} (black) and CO(3–2) (red) line profiles at selected outflow positions. CO line profiles, convolved to the H_2O spatial resolution, are scaled to match the H_2O line wings and the corresponding scaling factor is indicated in each plot. At the bottom of each spectrum, the relative H_2O/CO intensity ratio is plotted as a function of velocity.

depends on the type of grains involved and on the total density: for large grains, sputtering can be significantly inhibited for $n(H_2) \gtrsim 10^6$ cm^{-3}, due to the decrease of the relative velocity between grains and neutral species at these densities (Caselli et al. 1997). In fact, the observed SiO(8–7) emission gradually rises from the ambient velocity up to the EHV regime, a behavior that could suggest a progressive enhancement of the SiO abundance moving from the regime of high density and low velocity to that of low density and high velocity; the water, on the other hand, can be efficiently produced even at low shock speeds and high densities from sputtering of icy grain mantles, which would explain the different behavior of the two species in the intermediate velocity regime. However, the non-detection toward L1448-C of broad lines from other molecules that reside on ices, such as CH_3OH (Jiménez-Serra et al. 2005), is indicative of the fact that the gas/grain chemistry can indeed be more complex than normally assumed.

4. H_2O physical conditions and abundances

From the relative and absolute intensities of the observed H_2O lines, it is possible to derive spatially and spectrally averaged information about their excitation conditions. For this purpose, we convolved the PACS line map at the HIFI 557 GHz resolution

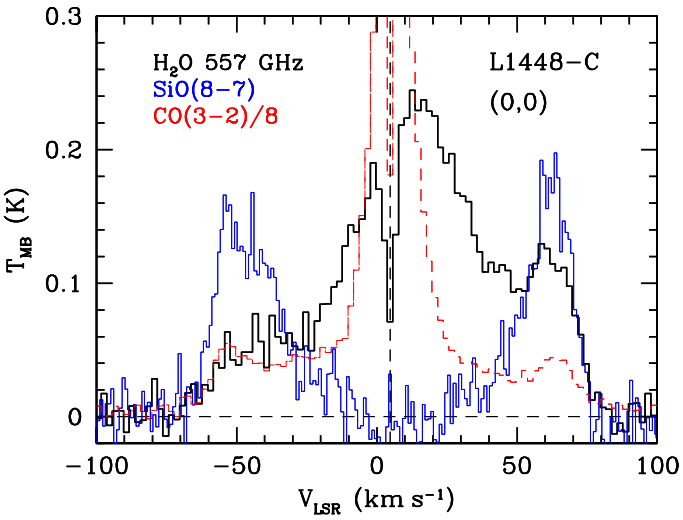

Fig. 6. Overlay between H_2O 1_{10}–1_{01} (black), SiO(8–7) (blue) and CO(3–2) (red) toward the L1448-C position.

(i.e. 38″) and integrated the HIFI spectra over velocity to compare line intensities for the same spatial and spectral regions. In Table 1, we report these intensities, as measured at different positions along the outflow, which correspond roughly to the water intensity peaks.

In Fig. 8, the 179 μm intensity is plotted as a function of the 179 μm /557 GHz ratio. Here the observed values are confronted with predictions obtained using the RADEX code (van der Tak et al. 2007) that we ran using the large velocity gradient (LVG) approximation in plane-parallel geometry. Based on the analysis presented in Santangelo et al. (2012), Vasta et al. (2012), and Bjerkeli et al. (2012), we assumed that the kinetic temperature ($T_{\rm kin}$) of the gas traced by the observed H_2O transitions is in the range 300–500 K, similar to that derived by Giannini et al. (2011) from *Spitzer* observations of the low-lying H_2 transitions. We then explored hydrogen densities ($n(H_2)$) in the range 10^5–10^7 cm^{-3} and o-H_2O column densities in the range 10^{12}–10^{16} cm^{-2}. A linewidth of 30 km s^{-1} was adopted, representing the typical FWHM of the observed 557 GHz line.

In Fig. 8 H_2O 179 μm intensities, convolved to the 557 GHz resolution, are indicated as open (cyan) symbols, while filled (red) symbols indicate the unconvolved PACS intensities. The convolved and unconvolved intensities differ by factors between 1.2 and 5, reflecting the extended but clumpy nature of the 179 μm emission as shown in Fig. 3. Assuming that the unconvolved intensities are not additionally diluted within the PACS beam, Fig. 8 suggests that the density of the gas responsible for the H_2O emission is in the range $\sim 10^6$–10^7 cm^{-3} while the H_2O column density is $\gtrsim 10^{13}$ cm^{-2}.

This result is consistent with the work of Santangelo et al. (2012), who analyzed *Herschel*-HIFI spectra of several H_2O lines gathered toward the L1448-R4 and B2 positions, concluding that the water emission in these positions arises from a gas at $T \sim$ 400–600 K and density of about $1–5 \times 10^6$ cm^{-3}. Models with densities lower than 10^6 cm^{-3} were not able to fit all lines observed with HIFI and would require high column densities that are inconsistent with the upper limit on the $H_2^{18}O$ observed in the L1448-R4 position. The conditions we derived are also consistent with the results obtained by Tafalla et al. (2012) from an analysis of the o-H_2O 1_{10}–1_{01} and 2_{12}–1_{01} emissions in a large sample of shocked spots.

In Fig. 9 the H_2O data are also compared with the CO(3–2) line intensity, which was convolved to the HIFI resolution. The expected 179 μm/CO(3–2) ratio was computed for N(CO) = 5×10^{15} cm^{-2}: this value assumes an average $N(H_2)$ column density of 5×10^{19} cm^{-2} along the flow (consistent with the column density estimated in Giannini et al. 2011) and a CO abundance of 10^{-4}. The figure shows that the observed data are reproduced by a single gas component only for $n(H_2) \sim 10^7$ cm^{-3} and $N(H_2O) < 10^{12}$ cm^{-2}. As shown above, these conditions are not consistent with intensities of the 179 μm emission. We also note that the assumed N(CO) is only an upper limit on the beam-diluted CO column density in the assumed 38″ aperture, since the $N(H_2)$ was estimated over a beam of size ∼10″. To be consistent with the observed ratios, a CO column density one or two order of magnitudes higher than that assumed here would be required, clearly inconsistent with the H_2 observations. This is further and more quantitative evidence that the CO(3–2) and the water emission originate from gas components with different excitation conditions. The low-J CO is likely related to the cold entrained gas and not directly associated with the high temperature shocked gas. Assuming that the CO emission originates in gas at a temperature of about 100 K and with a density of 10^4 cm^{-3} (e.g. van Kempen et al. 2009), the contribution of the H_2O 557 GHz emission from this gas would be negligible (i.e. 1/10 of the observed beam diluted intensity), even assuming a H_2O/CO abundance ∼1.

Assuming $T_{\rm kin} \sim$ 500 K and $n(H_2) \sim 5 \times 10^6$ cm^{-3}, o-H_2O beam-diluted PACS column densities are constrained to be about 10^{13} cm^{-2} along the flow, while a higher value of about 10^{14} cm^{-2} is inferred toward the central position (see Table 1). To estimate the corresponding H_2O abundance, we derived a $N(H_2)$ from the *Spitzer* spectral image of the H_2 S(1) 17 μm line (Neufeld et al. 2009; Giannini et al. 2011), on the assumption that it originates in the same gas as seen in H_2O by PACS. For this purpose, the H_2 17 μm image was convolved to the 12″ resolution of the PACS map, and the beam-averaged $N(H_2)$ was determined assuming the line to be in LTE with $T_{\rm kin}$ = 500 K. Values of $N(H_2)$ of about $0.7–6 \times 10^{19}$ cm^{-2} are derived for the different positions. Consequently, the water abundance along the outflow is relatively constant with values $\sim 0.5–1 \times 10^{-6}$ (see Table 1). For the on-source position, a higher value of $\sim 10^{-5}$ is found; however, the high on-source extinction might cause the $N(H_2)$ column density to be underestimated and consequently the $X(H_2O)$ to be overestimated. If we consider as a reference the H_2 S(0) 28 μm emission for deriving the $N(H_2)$ toward the central position, we obtain a value of $\sim 5 \times 10^{20}$ cm^{-2}, which would imply $X(H_2O) \sim 10^{-6}$. In this case, we should consider this value as a lower limit, since the S(0) emission is likely dominated by gas colder than that, giving rise to the water emission observed here.

We note that the derived abundances are sensitive to the adopted parameters and assumptions. In the regime considered here, the water column densities that we derive depend almost linearly on the assumed H_2 density, which we estimate to be uncertain by a factor of five. Changes in the assumed temperature, on the other hand, will affect both the H_2O and the H_2 column densities in a similar fashion, having less impact on the derived H_2O abundance.

5. Origin of the observed emission

Our analysis of the H_2O 1_{10}–1_{01} and 2_{12}–1_{01} lines suggests that the gas responsible for the bulk of the H_2O emission is warm, with $T_{\rm kin} \sim$ 300–500 K, and very dense, with

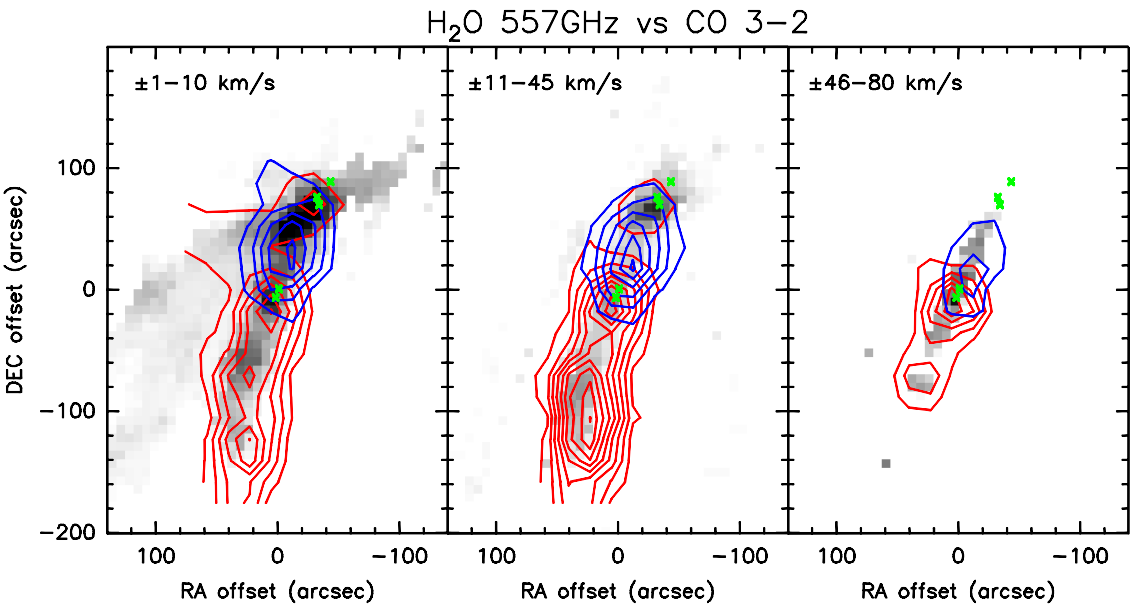

Fig. 7. Contours of the H_2O 1_{10}–1_{01} emission integrated in three different velocity intervals, superimposed onto the CO(3–2) emission in the same velocity bins (gray scale). The velocity ranges with respect to the systemic velocity of V_{LSR} = 4.7 km s^{-1}, are shown in the upper side of each panel. Green crosses mark the positions of the different sources (see Fig. 1).

Table 1. Line intensities* and H_2O abundances.

Position	$\int T_{mb}dv$ (K km s^{-1})			I(10^{-6} erg cm^{-2} s^{-1} sr^{-1})			N(o-H_2O)^b	X(H_2O)^c
($''$, $''$)^a	H_2O 1_{10}–1_{01}	H_2O 2_{21}–1_{01}	CO J = 3–2	H_2O 1_{10}–1_{01}	H_2O 2_{21}–1_{01}	CO J =3–2	10^{13} cm^{-2}	10^{-6}
(+26.0, −124.1)	10.3	3.2	32.9	1.78	14.9	1.3	3.0	...
(+29.3, −98.2)	7.5	2.8	31.6	1.30	12.9	1.3	1.3	0.7
(+23.4, −71.1)	10.4	2.7	61.3	1.80	12.6	2.5	1.6	0.8
(+11.1, −36.4)	7.9	2.4	26.9	1.37	11.0	1.1	1.0	2
(0, 0)	15.7	8.5	115.6	2.72	39.6	4.7	9.0	1–12.0
(−12.5, +34.9)	9.0	3.0	78.05	1.56	14.5	3.2	1.6	1
(−21.7, +63.9)	5.4	2.1	104.3	0.93	9.49	4.2	1.8	0.4

Notes. (*) Intensities measured in a circular area of diameter 38$''$. Absolute uncertainties are of about 20–30% for H_2O measurements and 15% for CO(3–2). (a) Offsets with respect to α_{2000} = 03:25:38.8, δ_{2000} = +30:44:04 (b) Derived from the unconvolved 2_{21}–1_{01} line intensity assuming T_{kin} = 500 K and $n(H_2) = 5 \times 10^6$ cm^{-3}. The associated uncertainty is within a factor of 5. (c) With respect to the H_2 column densities derived from the S(1) 17 μm line and assuming an o/p ratio of 3. Uncertainty on the abundance is within a factor of 10.

$n(H_2) \sim 5 \times 10^6$ cm^{-3}. These parameters, as well as the associated low abundance of $\lesssim 10^{-6}$, seem to be typical of the excitation traced by the two H_2O transitions, since similar physical conditions have been derived for other outflow positions by several authors (e.g. Bjerkeli et al. 2012; Vasta et al. 2012; Tafalla et al. 2012). These physical conditions, along with the observed spatial distribution of the 179 μm emission, indicate that these H_2O lines mainly trace gas that has been heated and compressed by shocks, rather than entrained ambient gas. This latter possibility was suggested by Franklin et al. (2008) on the basis of SWAS observations, but assuming the same physical parameters for the 557 GHz line as for the CO(1–0) line. In addition, our maps provided evidence that the excitation conditions and abundance of water in L1448 are fairly constant at the sampled spatial scales. This implies very similar shock properties, which seem to be unaffected by evolutionary effects on the timescales of the outflow propagation. The only exception is the region immediately adjacent to the protostar L1448-C: here an H_2O column density an order of magnitude higher is found relative to the other outflow positions. Part of this on-source emission is associated with the EHV jet where H_2O and SiO molecules might be directly synthesized in the atomic free protostellar wind (see also Kristensen et al. 2011).

The temperature of few hundred K inferred along the outflow is much lower than the maximum temperature of shocked molecular gas, as traced by H_2 near-IR rovibrational lines (~2000 K), for example. Far-IR H_2O lines at higher excitation observed by ISO in L1448 indicate the presence of hotter gas with $T \gtrsim$ 1000 K (Nisini et al. 1999, 2000), thus suggesting a distribution of gas temperatures similar to what has been inferred for the H_2 gas. PACS observations of several young sources suggest that the presence of gas components at different temperatures is indeed very common (e.g. Herczeg et al. 2011; Karska et al. 2012; Goicoechea et al. 2012) and that the H_2O abundance is typically higher in the hotter gas (Giannini et al. 2001; Santangelo et al. in prep.).

Considering excitation in a single shock, one can expect that different excitation components are associated with different layers in the post-shock region, and that the low-lying H_2O transitions considered here should trace post-shocked gas layers where

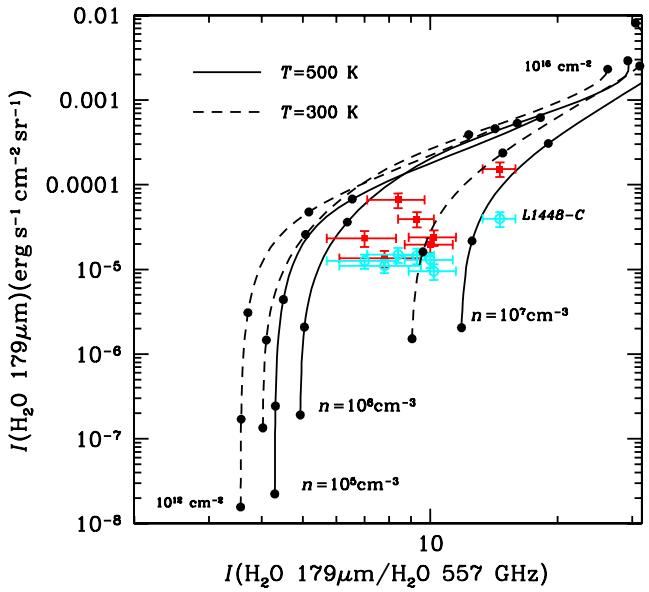

Fig. 8. H_2O 179 μm/557 GHz ratio vs. the H_2O 179 μm intensity (expressed in erg s^{-1} cm^{-2} sr^{-1}). Theoretical LVG predictions are plotted for volume densities of 10^5, 10^6 and 10^7 cm^{-3}, and for kinetic temperatures of 300 K (dashed line) and 500 K (full line). Along each curve the N(o-H_2O) column density varies from 10^{12} to 10^{16} cm^{-2} in steps of a factor 10. Open cyan circles refer to intensities measured in a beam of 38″, equal to the beam size of the 557 GHz observations. Filled red circles plot the *unconvolved* PACS intensities. The data point for L1448-C is labeled.

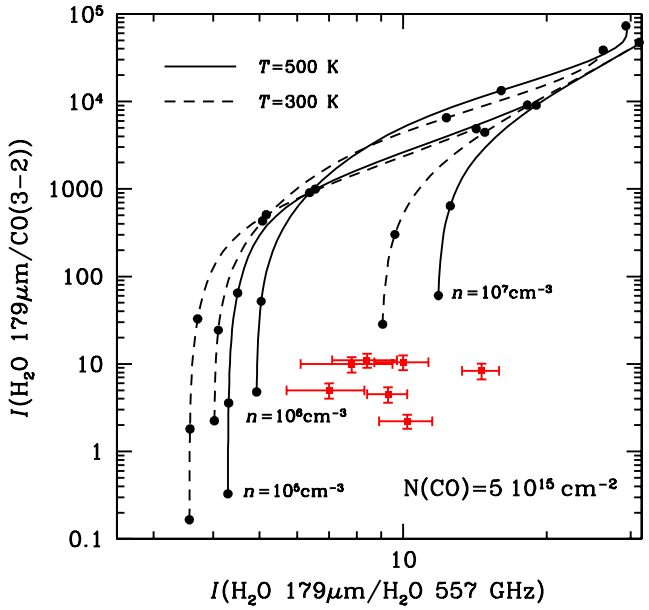

Fig. 9. Diagnostic diagram employing the H_2O 179 μm/557 GHz vs. the H_2O 179 μm/CO(3–2) intensity ratios. Theoretical LVG predictions are plotted for the same parameters as in Fig. 8. The plot assumes a fixed N(CO) column density of 5×10^{15} cm^{-2} (see text for details). Data points refer to intensities measured in a beam of 38″, equal to the beam of the 557 GHz observations.

the gas has already cooled down to a few hundred K. Santangelo et al. (2012) inferred that the ratios of low excitation H_2O lines in the L1448-B2 and R4 spots are consistent with nondissociative J-type shocks, a conclusion also supported by the high inferred densities, which imply a large shock compression factor. In these shocks, as also in C-shocks, high H_2O abundances are produced in the hot gas through the rapid conversion of atomic oxygen into water when $T_{\rm kin}$ exceeds ~300–400 K (Kaufman & Neufeld 2006; Flower & Pineau Des Forêts 2010), and should be maintained long after the gas has cooled down. Hence, we should measure the same high H_2O abundance in both the warm and the hot gas, unless the density is so high to allow a very quick freezeout of gas-phase water onto grain mantles.

For $n(H_2) \sim 10^6$ cm^{-3}, Bergin et al. (1996) derived a timescale ~10^4 yr for this process. Typical timescales for J-shock propagation at a pre-shock density of 10^4 cm^{-3} are shorter than 10^2 yr and the timescales are not longer than ~10^3 yr even for C-type shocks; hence grain freeze-out will be of minor importance in reducing the gas-phase water column density in the still warm regions of the post-shocked gas. A water abundance lower than that expected to result from endothermic gas-phase reactions could result if most of the oxygen not in CO is frozen out in ice mantles in the pre-shock gas. This possibility is strongly suggested by the very low abundance of O_2 gas as measured by SWAS and *Odin* in dense molecular clouds, which indicates that atomic oxygen could be largely depleted (Goldsmith et al. 2000; Larsson et al. 2007). However, ice mantles are quickly destroyed by sputtering for shock speeds exceeding ~10–15 km s^{-1}, so freeze-out within the pre-shock gas can be of relevance only for very slow shocks.

A different way to decrease the H_2O abundance in the post-shocked gas could be through photodissociation by a pre-existing far-ultraviolet (FUV) field. Shock regions located along the outflow cavity wall close to the protostar could be directly exposed to the central source FUV field (e.g. Visser et al. 2012). Far from the source, the only way to produce a significant FUV field is through fast J-type dissociative shocks. This scenario assumes a superposition of two shocks at different velocities: this is expected, e.g., in jet-driven outflows where a fast dissociative shock (i.e. the jet shock or Mach disk) decelerates the jet and a low-speed shock accelerates the ambient medium (e.g. Raga & Cabrit 1993). The effect of FUV photons, generated by a J-shock, impinging on the region behind a nondissociative shock has been discussed in Snell et al. (2005). Their result is that these photons are not effective in decreasing the abundance of the hot H_2O produced at the shock front, since here the timescales for H_2O formation are extremely short. However, in the post-shocked cooling region, water can be rapidly dissociated and consequently the H_2O abundance decreases significantly from the peak value at the shock front. Timescales for H_2O dissociation depend on the strength of the FUV field and the degree of FUV shielding (Lockett et al. 1999). Direct exposure to a radiation field with $G_0 >$ few × 10 (where G_0 is the intensity of the radiation field relative to its average interstellar value) returns all oxygen to atomic form very quickly. If the field is shielded by an $A_v \sim 1$ mag, timescales for converting H_2O back to oxygen are of about thousands of years and still compatible with the outflow dynamical timescale. Snell et al. determined that the column of post-shocked H_2O behind a C-type shock should scale with the FUV field as $\sim 4 \times 10^{15} (n_0/10^4 \text{ cm}^{-3})(v_s/10 \text{ km s}^{-1}) G_0^{-1}$, for a shock of velocity v_s in gas of pre-shock density 10^4 cm^{-3}. Our derived column densities of about 10^{14} cm^{-2} therefore imply the presence of a FUV field $G_0 \sim 25 (n_0/10^4 \text{ cm}^{-3})^{-1} (v_s/10 \text{ km s}^{-1})^{-1}$ cm^{-2} for such a shock. Additional modeling will be required to determine the exact properties of a J-shock capable of producing the necessary FUV field. However, the jet speed (with a projected velocity up to 80 km s^{-1} along the line of sight) is certainly high enough to drive a J-type shock that emits strongly at FUV wavelengths. A dissociative shock that gives rise to

ionizing photons is suggested, in at least specific positions, by the detection of [Fe II] emission along the L1448 outflow by Neufeld et al. (2009) and of OH emission toward the B2 clump (Santangelo et al. in prep.). Shocks close to the sources could instead be directly exposed to the source FUV field expanding in the envelope cavity, whose presence is revealed by the scattered light emission detected in the *Spitzer* IRAC images (Tobin et al. 2007). A different scenario can be also considered, where the hot and warm H_2O components are produced in two separate nondissociative shocks with different velocities. Slow C-type shocks with velocities $\lesssim$15 km s^{-1} produce post-shocked temperatures that never exceed ~300–400 K (e.g. Kaufman & Neufeld 1996): at these temperatures, the conversion of oxygen into water proceeds at very low efficiency and therefore the H_2O abundance does not dramatically increase relative to its to pre-shock value on the timescale of shock evolution. In addition, as discussed before, at these low velocities ice mantles are not efficiently sputtered; therefore the release of water from grains is also inhibited. This scenario would imply, however, that the bulk of the 557 GHz line that we observe originates in a shock with a speed much lower than the actual velocity as measured from the line profile.

6. Conclusions

H_2O 2_{12}–1_{01} and 1_{10}–1_{01} maps of the L1448 outflow were analyzed and compared with CO(3–2), SiO(8–7) and H_2 mid-IR lines to infer the origin and properties of H_2O emission in this prototypical class 0 outflow. The main results of our analysis can be summarized as follows:

- On the 12″ spatial scale provided by PACS, the 179 μm line distribution appears to be patchy, with emission peaks localized in shock spots along the outflow. Strong emission is observed toward the L1448-C source, which drives the main outflow in the region, whose spatial extent covers the collimated and compact molecular jet observed in the H_2 S(0) and S(1) lines.
- The kinematical information provided by the 557 GHz HIFI observations reveals that water lines trace the same velocity range as the CO gas, but present a remarkably different profile, which is dominated by emission at intermediate velocities (i.e. ±10–30 km s^{-1}). Emission from gas at extreme velocities (i.e. up to 80 km s^{-1}) is detected but it is not as prominent as in CO. We analyzed the velocity dependence of the H_2O/CO(3–2) ratio, finding that this ratio varies significantly with velocity. An initial H_2O/CO(3–2) increase is followed by a drop at velocity ~30 km s^{-1}. These velocity variations are indicative of strong changes in the physical and chemical conditions with the flow speed and cannot be explained by H_2O abundance variations alone.
- When compared with SiO(8–7) emission, detected in our map only close to the L1448-C source, H_2O emission presents significant kinematical differences. SiO is associated only with the EHV gas and is not detected from the broad H_2O emission component at intermediate velocity. The low H_2O/SiO ratio inferred in the EHV bullets is not reproduced by shock models and points to an origin from dust-free gas directly ejected from the protostellar wind. The absence of SiO in the broad H_2O component remains puzzling, however, and could be explained by assuming that grain disruption is inhibited in the very dense H_2O emitting region.
- From the H_2O observed line ratio and absolute intensities and from the additional constraints derived from H_2 lines observed with *Spitzer*, we infer that the gas responsible for the bulk of the water emission is warm, with $T_{\rm kin}$ ~ 300–500 K, and very dense, with $n_{\rm H_2} \sim 5\times10^6$ cm^{-3}. These parameters, as well as the association of the 179 μm emission with specific shock spots, indicate that these H_2O lines mainly trace gas that has been heated and compressed by shocks and not entrained ambient gas, which instead mainly contributes to the CO(3–2) emission.
- The H_2O abundance of the gas component traced by the 2_{12}–1_{01} and 1_{10}–1_{01} lines was directly measured comparing the H_2O column density with the H_2 column density inferred from the H_2 S(1) 17 μm line: values of about 0.5–1×10^{-6} are found, with small variations along the outflow, but these increase by roughly an order of magnitude toward the L1448-C source. This low abundance value, associated with warm gas at a few hundred K, suggests that a diffuse FUV field may act to dissociate the freshly formed water in the post-shock cooling regions. Alternative possibilities, such as H_2O formation in very low-velocity C-type shocks, or freeze-out of H_2O molecules on dust grains in the post-shocked gas, seem to provide a less compelling explanation of our findings.

Acknowledgements. The Italian authors gratefully acknowledge the support from ASI through the contract I/005/011/0. Astrochemistry in Leiden is supported by NOVA, by a Spinoza grant and grant 614.001.008 from NWO, and by EU FP7 grant 238258. The US authors gratefully acknowledge the support of NASA funding provided through an award issued by JPL/Caltech. HIFI has been designed and built by a consortium of institutes and university departments from across Europe, Canada and the United States under the leadership of SRON Netherlands Institute for Space Research, Groningen, The Netherlands and with major contributions from Germany, France and the US. Consortium members are: Canada: CSA, U. Waterloo; France: CESR, LAB, LERMA, IRAM; Germany: KOSMA, MPIfR, MPS; Ireland, NUI Maynooth; Italy: ASI, IFSI-INAF, Osservatorio Astrofisico di Arcetri-INAF; The Netherlands: SRON, TUD; Poland: CAMK, CBK; Spain: Observatorio Astronómico Nacional (IGN), Centro de Astrobiología (CSIC-INTA). Sweden: Chalmers University of Technology – MC2, RSS & GARD; Onsala Space Observatory; Swedish National Space Board, Stockholm University – Stockholm Observatory; Switzerland: ETH Zurich, FHNW; USA: Caltech, JPL, NHSC. PACS has been developed by a consortium of institutes led by MPE (Germany) and including UVIE (Austria); KU Leuven, CSL, IMEC (Belgium); CEA, LAM (France); MPIA (Germany); INAF-IFSI/OAA/OAP/OAT, LENS, SISSA (Italy); IAC (Spain). This development has been supported by the funding agencies BMVIT (Austria), ESA-PRODEX (Belgium), CEA/CNES (France), DLR (Germany), ASI/INAF (Italy), and CICYT/MCYT (Spain).

References

Bachiller, R., Martin-Pintado, J., Tafalla, M., Cernicharo, J., & Lazareff, B. 1990, A&A, 231, 174
Bachiller, R., Martin-Pintado, J., & Fuente, A. 1991, A&A, 243, L21
Bachiller, R., Guilloteau, S., Dutrey, A., Planesas, P., & Martin-Pintado, J. 1995, A&A, 299, 857
Benedettini, M., Viti, S., Giannini, T., et al. 2002, A&A, 395, 657
Benedettini, M., Busquet, G., Lefloch, B., et al. 2012, A&A, 539, L3
Bergin, E. A., Neufeld, D. A., & Melnick, G. J. 1998, ApJ, 499, 777
Bjerkeli, P., Liseau, R., Olberg, M., et al. 2009, A&A, 507, 1455
Bjerkeli, P., Liseau, R., Nisini, B., et al. 2011, A&A, 533, A80
Cabrit, S., Codella, C., Gueth, F., et al. 2007, A&A, 468, L29
Caselli, P., Hartquist, T. W., & Havnes, O. 1997, A&A, 322, 296
Ceccarelli, C., Caux, E., White, G. J., et al. 1998, A&A, 331, 372
Codella, C., Cabrit, S., Gueth, F., et al. 2007, A&A, 462, 53
Codella, C., Ceccarelli, C., Nisini, B., et al. 2010a, A&A, 522, L1
Codella, C., Lefloch, B., Ceccarelli, C., et al. 2010b, A&A, 518, L112
Davis, C. J., & Smith, M. D. J. 1996, A&A, 309, 929
de Graauw, T., Helmich, F. P., Phillips, T. G., et al. 2010, A&A, 518, L6
Dent, W., Duncan, W., Ellis, M., et al. 2000, Imaging at Radio through Submillimeter Wavelengths, 217, 33
Dionatos, O., Nisini, B., Cabrit, S., Kristensen, L., & Pineau Des Forêts, G. 2010, A&A, 521, A7
Dutrey, A., Guilloteau, S., & Bachiller, R. 1997, A&A, 325, 758
Flower, D. 2010, Lecture Notes in Physics (Berlin: Springer Verlag), 793, 161
Flower, D. R., & Pineau Des Forêts, G. 2010, MNRAS, 406, 1745

Franklin, J., Snell, R. L., Kaufman, M. J., et al. 2008, ApJ, 674, 1015
Giannini, T., Nisini, B., & Lorenzetti, D. 2001, ApJ, 555, 40
Giannini, T., Nisini, B., Neufeld, D., et al. 2011, ApJ, 738, 80
Girart, J. M., & Acord, J. M. P. 2001, ApJ, 552, L63
Glassgold, A. E., Mamon, G. A., & Huggins, P. J. 1991, ApJ, 373, 254
Goicoechea, J. R., Cernicharo, J., Karska, A., et al. 2012, A&A, 548, A77
Goldsmith, P. F., Melnick, G. J., Bergin, E. A., et al. 2000, ApJ, 539, L123
Guilloteau, S., Bachiller, R., Fuente, A., & Lucas, R. 1992, A&A, 265, 49
Gusdorf, A., Pineau Des Forêts, G., Cabrit, S., & Flower, D. R. 2008, A&A, 490, 695
Herczeg, G. J., Karska, A., Bruderer, S., et al. 2012, A&A, 540, A84
Hirano, N., Liu, S.-Y., Shang, H., et al. 2006, ApJ, 636, L141
Hirano, N., Ho, P. P. T., Liu, S.-Y., et al. 2010, ApJ, 717, 58
Hirota, T., Honma, M., Imai, H., et al. 2011, PASJ, 63, 1
Jiménez-Serra, I., Martín-Pintado, J., Rodríguez-Franco, A., & Martín, S. 2005, ApJ, 627, L121
Jiménez-Serra, I., Caselli, P., Martín-Pintado, J., & Hartquist, T. W. 2008, A&A, 482, 549
Jørgensen, J. K., Harvey, P. M., Evans, N. J., II, et al. 2006, ApJ, 645, 1246
Kaufman, M. J., & Neufeld, D. A. 1996, ApJ, 456, 611
Karska, A., Herczeg, G. J., van Dishoeck, E. F., et al. 2012, A&A, submitted
Kristensen, L. E., van Dishoeck, E. F., Tafalla, M., et al. 2011, A&A, 531, L1
Kristensen, L. E., van Dishoeck, E. F., Bergin, E. A., et al. 2012, A&A, 542, A8
Kwon, W., Looney, L. W., Crutcher, R. M., & Kirk, J. M. 2006, ApJ, 653, 1358
Langer, W. D., & Glassgold, A. E. 1990, ApJ, 352, 123
Larsson, B., Liseau, R., Pagani, L., et al. 2007, A&A, 466, 999
Lefloch, B., Cabrit, S., Codella, C., et al. 2010, A&A, 518, L113
Liseau, R., Ceccarelli, C., Larsson, B., et al. 1996, A&A, 315, L181
Lockett, P., Gauthier, E., & Elitzur, M. 1999, ApJ, 511, 235
Looney, L. W., Mundy, L. G., & Welch, W. J. 2000, ApJ, 529, 477
Neufeld, D. A., Nisini B., Giannini T., et al. 2009, ApJ, 706, 170
Nisini, B., Benedettini, M., Giannini, T., et al. 1999, A&A, 350, 529
Nisini, B., Benedettini, M., Giannini, T., et al. 2000, A&A, 360, 297
Nisini, B., Codella, C., Giannini, T., et al. 2007, A&A, 462, 163
Nisini, B., Giannini, T., Neufeld, D. A., et al. 2010, ApJ, 724, 69
Panoglou, D., Cabrit, S., Pineau Des Forêts, G., et al. 2012, A&A, 538, A2
Pickett, H. M., Poynter, R. L., Cohen, E. A., et al. 1998, J. Quant. Spec. Radiat. Transf., 60, 883
Pilbratt, G. L., Riedinger, J. R., Passvogel, T., et al. 2010, A&A, 518, L1
Poglitsch, A., Waelkens, C., Geis, N., et al. 2010, A&A, 518, L2
Raga, A., & Cabrit, S. 1993, A&A, 278, 267
Roelfsema, P. R., Helmich, F. P., Teyssier, D., et al. 2012, A&A, 537, A17
Santangelo, G., Nisini, B., Giannini, T., et al. 2012, A&A, 538, A45
Smith, H., Buckle, J., Hills, R., et al. 2008, in Proc. SPIE, 7020
Snell, R. L., Hollenbach, D., Howe, J. E., et al. 2005, ApJ, 620, 758
Tafalla, M., Santiago-García, J., Hacar, A., & Bachiller, R. 2010, A&A, 522, A91
Tafalla, M., Liseau, R., Nisini, B. et al., 2012, A&A, submitted
Tobin, J. J., Looney, L. W., Mundy, L. G., Kwon, W., & Hamidouche, M. 2007, ApJ, 659, 1404
van der Tak, F. F. S., Black, J. H., Schöier, F. L., Jansen, D. J., & van Dishoeck, E. F. 2007, A&A, 468, 627
van Dishoeck, E. F., Kristensen, L. E., Benz, A. O., et al. 2011, PASP, 123, 138
Vasta, M., Codella, C., Lorenzani, A., et al. 2012, A&A, 537, A98

Pages 13 to 15 are available in the electronic edition of the journal at http://www.aanda.org

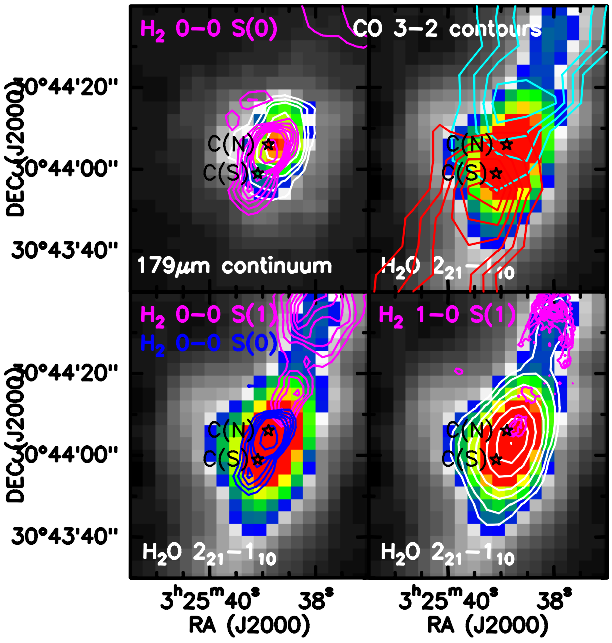

Fig. A.1. Maps of the 179 μm line and continuum emission in the region around L1448-C sources, compared with CO(3–2) and H_2 lines at different excitation, namely the 0–0 S(0)(28 μm), 0–0 S(1)(17 μm), and 1–0 S(1)(2.12 μm). White contours, shown in the *bottom right* and *upper left panels*, for the line and continuum emission respectively, are drawn at the following values: 1.5, 2.0, 3.0, 4.0, 6.0 8.0 $\times$ 10^{-5} erg s^{-1} cm^{-2} sr^{-1} for the line emission, and 0.6, 0.8, 1.2, 1.6 $\times$ 10^{-3} erg s^{-1} cm^{-2} sr^{-1} for the continuum emission.

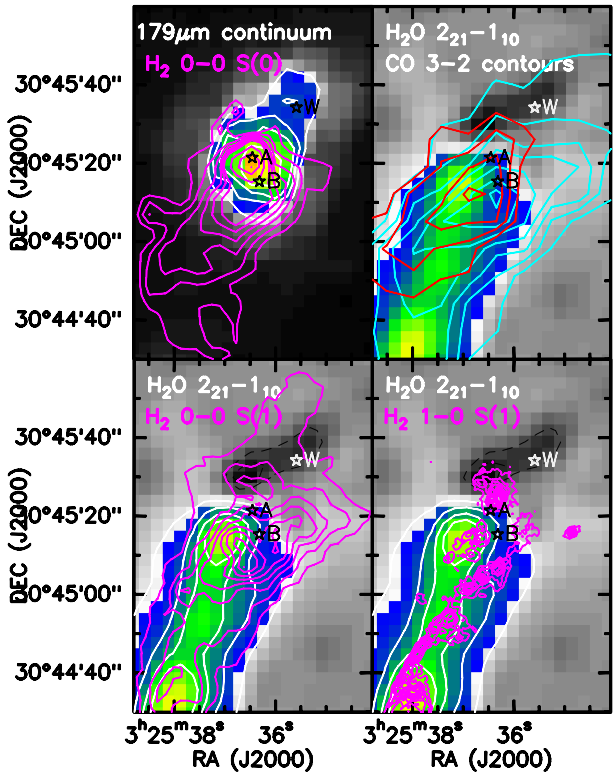

Fig. A.2. Same as Fig. A.1 for a region around L1448-N. In this case, white contours are drawn for the line and continuum emission with the following values: 0.6, 1.2, 1.8, 2.4, 4.0 $\times$ 10^{-5} erg s^{-1} cm^{-2} sr^{-1} (line) and 0.6, 0.8, 1.2, 1.6 $\times$ 10^{-3} erg s^{-1} cm^{-2} sr^{-1} (continuum). A contour of black broken line delineates the absorption region.

Appendix A: Comparison of different tracers around the L1448-C and N regions

A.1. L1448-C

Figure A.1 shows an enlargement of the 179 μm emission in the region around L1448-C. Both the continuum and the H_2O emission are displayed, with superimposed contours of the CO(3–2) and different H_2 lines (near-IR, from Davis & Smith 1996, and *Spitzer* from Giannini et al. 2011). The 179 μm line peaks toward the C(N) source but is elongated along the direction of the molecular jet, as discussed in Sect. 4.1, which in the figure is traced by the H_2 0–0 S(0) and S(1) lines and comprises the inner peaks in the CO(3–2) emission. The H_2 S(0) line is observed on source and along the SE (redshifted) jet, while the S(1) line is detected only toward the NW blueshifted jet and toward the B1 region. Extinction is the likely reason why the S(1) line is not detected on-source. Assuming a temperature of about 300 K, the ratio between the S(0) flux and the S(1) upper limit implies a lower limit of $A_v \sim 65$ mag toward the source and 45 mag in the redshifted jet.

Finally, Fig. A.1 shows the overlay with the H_2 2.12 μm line. At the central source position the line is almost totally extincted and thus no NIR emission is associated with the jet. The 2.12 μm line emission traces instead a bow shock in the blue lobe originated in the interaction of the jet with the ambient medium, which also shows up also as a clump of H_2O emission.

A.2. L1448-N

The 179 μm continuum image, displayed in Fig. A.2, shows unresolved emission from the three sources of the L1448-N cluster, whose peak coincides with the N(A) source. The H_2 S(0) emission, overlaid on the continuum image, also peaks toward N(A), indicating large columns of cold gas. As described in Sect. 3.1, only two of the three sources power outflows, resolved through interferometric observations by Girart et al. (2001) and Kwon et al. (2006). The outflow from N(A) is very compact and is seen almost perpendicular to the line of sight. By contrast, the outflow from N(B) is more elongated and extends to about 100″ from the driving source (at PA = 110°) both in the blue- and redshifted lobes. In our CO map we cannot distinguish the blueshifted gas of these two outflows from the large-scale L1448-C main outflow; however, we identify redshifted emission at velocity between ~+1 and +20 km s^{-1} mainly originating from the N(B) flow (see also Fig. 3, left).

In contrast with L1448-C, the 179 μm line emission does not peak toward the sources of this region, but is associated only with the outflow: bright emission is, in particular, observed close to the H_2 S(1) and to the CO(3–2) redshifted peaks. The bulk of the water emission, however, does not follow the curving H_2 large-scale jet driven by L1448-C, but seems to be associated with the 2.12 μm H_2 emission (knots Y/Z in Davis & Smith 1996), excited in the L1448-N(A/B) outflows. This could be a density effect, if one assumes that the density at the base of the N(A/B) flows is higher than the gas along the large-scale jet.

North of the N(A/B) sources the water emission decreases abruptly, while an absorption line of water appears, that follows the 179 μm continuum. The water absorption region lies along the line of sight of the L1448-N reflection nebula, visible in the IR images at both 2.12 μm and in the *Spitzer* IRAC maps (Davis & Smith 1996; Tobin et al. 2007). This evidence suggests that the cold water in the blueshifted outflow is seen in absorption against the nebula, which therefore lies in the background.

Appendix B: H_2O 557 GHz spectra and velocity channel maps

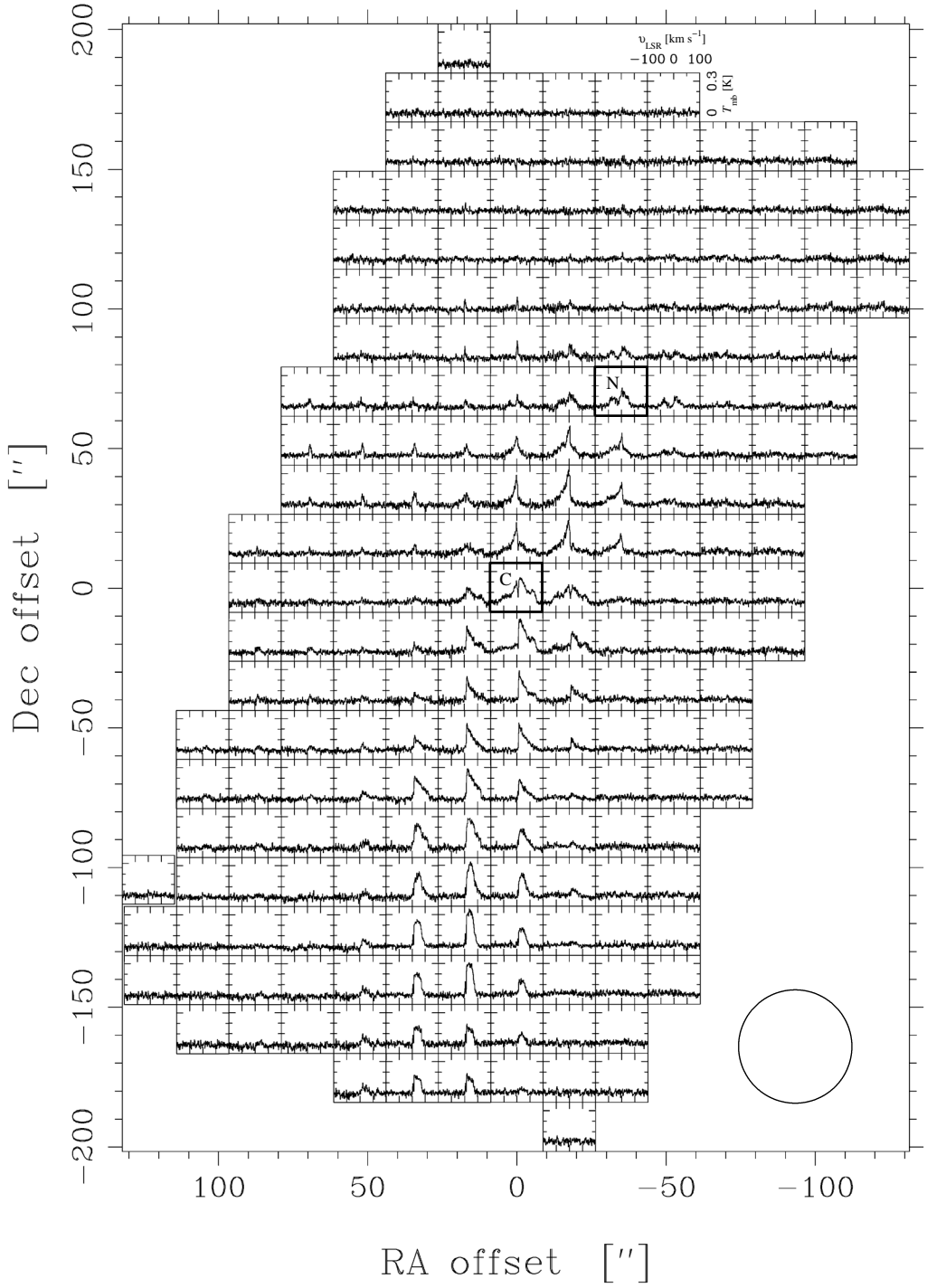

Fig. B.1. HIFI map of the H_2O $1_{10}-1_{01}$ 557 GHz line. The data have been regridded onto a regular grid of 18″ of spacing (i.e. half of the instrumental HPBW, which is displayed in the figure as reference) and binned at 1 km s^{-1} resolution. The map is centered on the L1448-C source at α_{2000} = 03^{h}25^{m}38.4^s, δ_{J2000} = +30°44′06″.

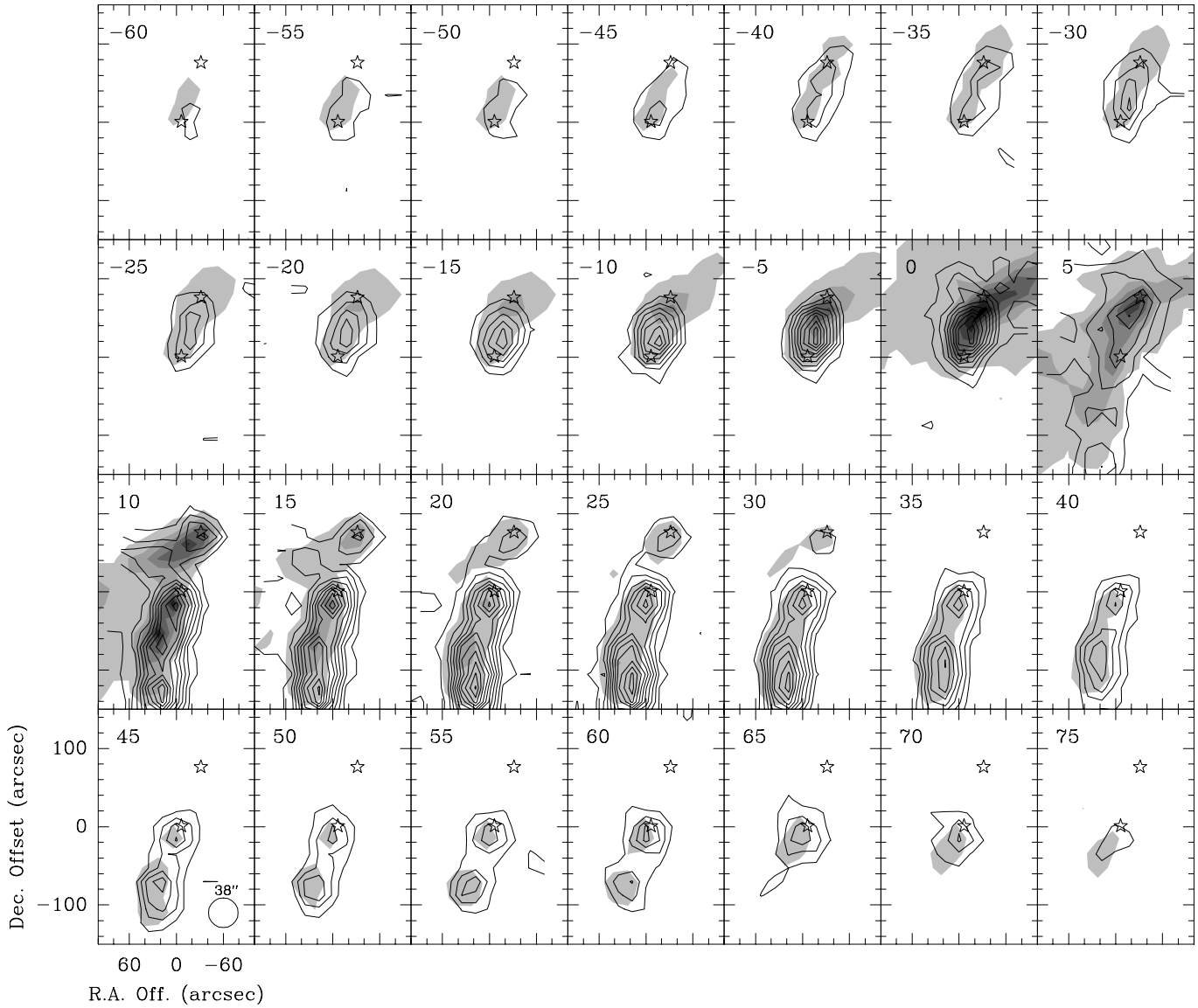

Fig. B.2. Contours of integrated H_2O 557 GHz intensities in velocity intervals of ΔV = 5 km s^{-1} superimposed on gray-scale maps of the CO(3–2) intensity integrated in the same bins. The center velocity of the bins is indicated in each panel. H_2O contours are in steps of 0.03 K km s^{-1} and the first contour is at 0.03 K km s^{-1} (equivalent to 3σ), while CO gray levels are in steps of 1.2 K km s^{-1} and the first contour is at 0.2 K km s^{-1}. The starred symbols represent the positions of the L1448-C and L1448-N sources.